Next Materials 12 (2026) 102264

Contents lists available at ScienceDirect

Next Materials

journal homepage: www.sciencedirect.com/journal/next-materials

Research article

High-performance supercapacitor based on cobalt nanostructures directly grown on engineered nickel foam substrate with enhanced ion transport and cycling stability

Ioannis Poimenidis [a,*], Kamil Bochenek [b,c], Aliaksandr Martsinchyk [c], Karolina Majewska [c], Pavel Shuhayeu [c], Jarosław Milewski [c], Michalis Konsolakis [a,*]

[a] Lab of Materials Science and Processes, School of Production Engineering & Management, Technical University of Crete, Crete, Chania 73100, Greece
[b] Institute of Fundamental Technological Research, Polish Academy of Sciences, Pawińskiego 5B, Warsaw 02-106, Poland
[c] Faculty of Power and Aeronautical Engineering Warsaw University of Technology, 21/25 Nowowiejska street, Warsaw 00-665, Poland

ARTICLE INFO

Keywords:
Cobalt oxide
Symmetric supercapacitor
Cycling stability
Tailored Nickel foam
Pseudocapacitor behavior

ABSTRACT

The electrochemical performance of cobalt-based supercapacitor electrodes is often limited by the relatively smooth surface of pristine nickel foam substrates. To overcome this limitation, a microstructurally engineered nickel foam scaffold was fabricated by introducing a porous nickel microparticle interlayer via screen printing. Cobalt nanostructures were hydrothermally grown on the modified substrate, forming a hierarchical electrode (Co@NF-M), which was systematically compared with electrodes prepared on commercial nickel foam (Co@NF). Structural and spectroscopic analyses supported the formation of predominantly crystalline spinel Co_3O_4, characterized by mixed Co^{2+}/Co^{3+} oxidation states. Morphological analysis further demonstrated a porous cobalt nanostructure anchored onto a roughened nickel scaffold, providing abundant active sites and facilitating electrolyte penetration and ion diffusion. Electrochemical impedance spectroscopy indicated a reduced charge-transfer resistance and improved electron transport compared to the conventional Co@NF electrode. As a result, the Co@NF-M electrode exhibited superior electrochemical performance, delivering specific capacitances of 1278, 1184, 1003, and 602 F g^{-1} at 0.5, 1, 5, and 10 A g^{-1}, respectively. Furthermore, the symmetric Co@NF-M//Co@NF-M device retained 95% of its initial capacitance after 3000 cycles, demonstrating excellent cycling stability. The enhanced performance is attributed to the engineered nickel scaffold, which promotes more uniform cobalt growth and improves interfacial contact while facilitating electron and ion transport.

1. Introduction

The increasing global energy demand and depletion of fossil fuels have intensified the search for efficient and sustainable energy storage technologies to complement renewable energy systems such as solar and wind. Although these sources are clean and abundant, their intermittent nature necessitates high-performance energy storage devices capable of delivering both high energy and power densities. In this context, electrochemical supercapacitors (SCs) have attracted significant attention owing to their fast charge-discharge performance, long cycle life, and high power density, effectively bridging the gap between conventional capacitors and batteries [1–3].

SCs are broadly classified into electric double-layer capacitors (EDLCs) and pseudocapacitors (PCs) based on their charge storage mechanisms. EDLCs rely on electrostatic charge accumulation at the electrode-electrolyte interface, typically employing carbon-based materials such as activated carbon, graphene, and carbon nanotubes [1,3,4]. In contrast, pseudocapacitors store energy through rapid, reversible Faradaic redox reactions occurring at or near the electrode surface, often using transition metal oxides, hydroxides, or conductive polymers [5,6]. Among these, transition metal oxides are particularly promising because of their multiple oxidation states, tunable crystal structures, and high theoretical capacitance [5,7].

Cobalt oxide (Co_3O_4), a spinel-type transition metal oxide, has emerged as one of the most promising pseudocapacitive materials because of its mixed-valence Co^{2+}/Co^{3+} redox system, chemical stability, and high theoretical capacitance [8,9]. These properties enable multiple Faradaic reactions that contribute to the high charge-storage

* Corresponding authors.
E-mail addresses: ipoimenidis@tuc.gr (I. Poimenidis), mkonsolakis@tuc.gr (M. Konsolakis).

https://doi.org/10.1016/j.nxmate.2026.102264
Received 3 April 2026; Received in revised form 8 May 2026; Accepted 10 May 2026
Available online 15 May 2026

capability. However, the relatively low intrinsic electrical conductivity of Co_3O_4 and its limited ion diffusion kinetics can restrict its rate capability and cycling stability. To address these limitations, considerable research efforts have focused on the direct growth of Co_3O_4 nanostructures on conductive substrates, thereby creating electrodes with improved electrical contact, enhanced mechanical stability, and efficient ion transport pathways [10,11].

Nickel foam (NF) is one of the most widely used conductive scaffolds for such electrodes because of its highly porous three-dimensional architecture, excellent electrical conductivity, and mechanical robustness [4,12]. The open porous network facilitates electrolyte penetration and short diffusion pathways while maintaining continuous electronic conduction throughout the electrode structure [5]. Nevertheless, the surface of commercial NF is relatively smooth and partially covered by passive oxide layers, which can limit the nucleation density and uniform growth of electroactive materials, potentially weakening the interfacial contact between the active phase and metallic substrate.

To address these limitations, several NF modification strategies have been reported, including acid etching [13], electrodeposition [14,15], chemical plating [16], and plasma treatment [17,18]. These methods can improve surface roughness [17,19–21], surface activity [17,22], or coating adhesion [19,23]; however, they may also present disadvantages such as limited control over interlayer thickness [16] and uniformity [13,24], multistep processing [21,23], the requirement for specialized instrumentation [17,20,21], or reduced suitability for large-area fabrication [25]. Therefore, the development of a simple, scalable, and controllable NF pre-engineering strategy remains highly relevant for advanced Co_3O_4/NF-based electrodes.

Engineering the surface properties of metallic scaffolds has emerged as an effective strategy for improving the performance of electrodes. It is well established that the electrochemical performance of supercapacitor electrodes is strongly influenced by their structural architecture, with hierarchical porous structures significantly enhancing electrolyte accessibility, increasing active surface area, and facilitating rapid ion diffusion [26]. In particular, increasing the surface roughness and introducing micro/nanostructured features can significantly increase the number of active sites and promote more uniform nucleation of the deposited material [27]. In addition, improving the physical contact between the deposited oxide layer and the conductive scaffold can reduce the interfacial resistance and facilitate efficient electronic transport throughout the electrode framework [28]. Introducing a porous metallic interlayer can further increase the density of mechanical anchoring sites and improve the electrolyte accessibility within the porous structure [6]. Among the available modification approaches, screen printing offers several practical advantages for substrate engineering, including low processing cost, compatibility with scalable manufacturing, and the possibility of controlling the thickness and composition of the deposited interlayer [29,30]. In addition, the printed metallic layer can act as a mechanically robust transition region between the substrate and the subsequently grown active phase, thereby improving the interfacial adhesion and structural integrity during electrochemical cycling.

At the same time, the structural properties of cobalt oxide coatings strongly depend on synthesis parameters such as precursor concentration, reaction temperature, and reaction time [31,32]. These parameters influence the crystallinity, phase composition, and microstructural characteristics of the resulting cobalt-based nanostructures, which, in turn, affect charge-transfer kinetics and pseudocapacitive behavior. In particular, the coexistence of metallic Co and spinel Co_3O_4 has been reported to enhance the electrochemical performance, as metallic Co improves the electrical conductivity, while the Co_3O_4 phase provides abundant redox-active sites [33].

In this study, a modified nickel foam substrate was developed prior to cobalt deposition to tailor the substrate microstructure and improve the integration of the active material with the conductive scaffold. A porous nickel-based intermediate layer was fabricated on commercial NF by screen-printing Ni-255 powder with a polymer-assisted binder system, yielding a modified substrate (NF-M) with increased surface roughness and a higher density of anchoring sites. This engineered substrate promotes the formation of a cobalt nanostructure network and enhances the physical contact between the cobalt-based coating and metallic framework. In contrast to conventional Co_3O_4@NF architectures, where nickel foam is typically used directly or modified by more conventional surface-treatment routes, the present approach employs a deliberately pre-engineered screen-printed Ni interlayer that enables better control of the substrate microstructure, nucleation behavior, and interface quality prior to hydrothermal cobalt growth.

The resulting Co@NF-M electrode exhibits enhanced electrochemical performance, arising from the combined contributions of the crystalline Co_3O_4 nanostructures and the engineered nickel substrate, which facilitates efficient electron transport and improved interfacial contact. Electrochemical measurements reveal a high specific capacitance and excellent cycling stability of the Co@NF-M electrode. Furthermore, a symmetric Co@NF-M//Co@NF-M device demonstrates competitive energy and power densities with stable long-term performance, highlighting the effectiveness of the integrated electrode architecture for advanced supercapacitor applications.

The novelty of this work lies in the synergistic two-step fabrication strategy used to construct the electrode, in which a commercial nickel foam is first pre-engineered by screen-printing a porous Ni microparticle interlayer and then used as a scaffold for the in situ hydrothermal growth of cobalt-based nanostructures. Compared with conventional Co_3O_4@NF architectures, this approach offers a more controllable route for substrate modification, combining low-cost and scalable processing with improved interlayer design, enhanced nucleation-site density, stronger interfacial adhesion, and more efficient electron/ion transport. To the best of our knowledge, the deliberate coupling of screen-printed NF pre-engineering with subsequent hydrothermal cobalt growth has remained largely unexplored for supercapacitor electrodes. This strategy not only improves the electrochemical performance but also provides a scalable, cost-effective pathway for the rational design of advanced NF-based electrodes for practical supercapacitor applications.

2. Experimental section

2.1. Materials

All the materials in this study were used as received without further purification: potassium hydroxide (KOH, technical grade, Sigma-Aldrich), ethanol (CH_3CH_2OH 99.8%, ACROS Organics), hydrochloric acid (HCl 98% Sigma Aldrich), cobalt(II) nitrate hexahydrate ($Co(NO_3)_2{\cdot}6H_2O$, 98% Sigma Aldrich), nickel foam (99.8%, Changzhou DLX Alloy Co, 90% porosity, 90 ppi), nickel powder (Vale Type 255, 99.9%, Fisher sub sieve size 2.2–2.6 μm), polyvinyl alcohol (PVA, Sigma Aldrich), polyacrylic acid (PAA, Sigma Aldrich), and Polyethylene glycol (PEG, Sigma Aldrich).

2.2. Fabrication of modified Ni foam substrate (NF-M)

To enhance the nucleation and adhesion of cobalt nanostructures, the nickel foam substrate was intentionally modified by introducing a porous nickel microparticle interlayer fabricated by screen printing. In particular, modified nickel-based electrodes (NF-M) were manufactured by screen printing with a water-soluble polymer binder and high-purity nickel powder was used. The objective was to obtain mechanically stable porous structures with controlled microstructures. The ink formulation process began by dissolving polyvinyl alcohol and polyacrylic acid in deionized water to form a binder-dispersant system. The solution was heated gently (ca. 70 °C) to ensure complete dissolution of the polymers, and then cooled to ambient temperature. Polyethylene glycol was added as a viscosity modifier and plasticizer to improve the printability and flexibility of the green layers. High-purity nickel powder was slowly

introduced into the prepared binder solution under mechanical stirring. The resulting slurry was mixed under vacuum at 250 rpm for 2 h to remove entrapped air and promote homogeneity, and then manually applied to a porous nickel foam via screen printing to form a thin Ni-255/polymer layer. The printed layers were then dried under ambient conditions (room temperature) for 24 h to obtain the fabricated substrate (NF-M) for subsequent Co deposition.

2.3. Hydrothermal fabrication of Co@NF

The hydrothermal fabrication of Co_xO_y electrodes over commercial NF and NF-M has been described in our previous work [14,34]. Briefly, 16 mmol of $Co(NO_3)_2{\cdot}6\ H_2O$ was dissolved in 40 mL of absolute ethanol. The obtained solution and NF or NF-M substrates were then transferred into a Teflon-lined stainless-steel autoclave and heated at 120 °C for 10 h. Subsequently, the electrodes Co@NF and Co@NF-M were washed several times with deionized water and ethanol, dried at 60 °C for 12 h, and calcined in air at 300 °C for 3 h (heating rate: 5 °C/min). The loading of the cobalt species was approximately 6 ± 0.2 mg cm^{-2}, calculated based on the geometric area of the electrode. The cobalt loading was determined gravimetrically by measuring the mass of the nickel foam substrate before and after hydrothermal growth using an analytical balance.

2.4. Symmetric supercapacitor fabrication

To fabricate the symmetric supercapacitor, two Co@NF-M electrodes were employed as both the positive and negative electrodes. A Millipore membrane (XDF-DL, China) served as the separator. A 2 M KOH aqueous electrolyte was employed owing to its high ionic conductivity and sufficient OH^- availability, which facilitates rapid Faradaic redox reactions in cobalt-based electrodes. This concentration is widely used in alkaline supercapacitor systems [35,36]. The assembly was carried out in a custom-designed cell constructed with plexiglass gaskets and EPDM rubber to ensure effective sealing.

2.5. Materials characterization

X-ray diffraction (XRD) patterns were obtained using a Rigaku MiniFlex II diffractometer with Cu Kα radiation (λ = 1.5406 Å), operated at 30 kV and 15 mA, to elucidate the structural characteristics and chemical composition of the fabricated electrodes. In addition, field-emission scanning electron microscopy (FE-SEM, Zeiss Crossbeam 350) at various magnifications was used to characterize the morphology of the fabricated electrodes, and X-ray spectroscopy (EDAX) was used to analyze the elemental composition. Additionally, a Quantachrome Instruments AutoSorbiQ analyzer was employed to conduct nitrogen adsorption-desorption measurements, with N_2 adsorption at −196 °C and data processed using ASQWIN software. X-ray photoelectron spectroscopy (XPS) measurements were conducted using a SPECS FlexMod system equipped with a monochromatic Al Kα source (hν = 1486.6 eV). Survey and high-resolution core-level spectra were acquired at pass energies of 100 eV and 20 eV, respectively. All binding energies were calibrated with respect to the C 1 s peak at 284.8 eV.

2.6. Electrochemical measurements

A series of electrochemical tests, including cyclic voltammetry (CV) at varying scan rates, galvanostatic charge-discharge (GCD), electrochemical impedance spectroscopy (EIS), and long-term cycling stability, were performed to evaluate the kinetic behavior, capacitive performance, and charge storage capability of the electrodes. The specific capacitance values were calculated from the obtained data. The electrochemical responses of NF-M were measured as a reference electrode to demonstrate the negligible capacitance contribution of the substrate compared with that of the cobalt-loaded electrodes. The measurements were performed using a VersaSTAT 4 electrochemical workstation configured with a standard three-electrode system in a 2 M KOH aqueous electrolyte. The setup employed a platinum foil as the counter electrode, a standard calomel electrode (SCE) as the reference electrode, and the prepared electrodes as the working electrodes. A two-electrode setup was employed in a symmetric capacitor configuration, and the tests described above were conducted. Additionally, to assess the reproducibility of the as-prepared electrodes, three samples of each electrode type were fabricated and tested.

3. Results and discussion

3.1. Morphological and structural characterization

The microstructural evolution before and after cobalt deposition was examined using FE-SEM (Fig. 1). The pristine NF-M substrate (Fig. 1a-c) exhibits a dense, compact morphology composed of irregularly shaped Ni particles, while the commercial NF (Fig. 1a inset) shows a relatively smooth surface. After the hydrothermal deposition of Co on the NF-M substrate, the surface morphology was notably modified (Fig. 1d-e). A dense layer of cobalt-based nanostructures was grown on a Ni framework, forming interconnected nanosheets that assembled into a porous, flower-like architecture. This hierarchical surface significantly increases the electrochemically active area (see below) and provides open channels for electrolyte ion transport [37].

In contrast, cobalt deposition on commercial nickel foam (Co@NF, Fig. 1g-i) yielded a less homogeneous distribution of nanostructures, with locally aggregated cobalt domains and incomplete surface coverage.

ImageJ was used to quantify the SEM images (Table S1) and assess the interparticle void distribution across various electrodes. The NF-M substrate displayed an average diameter of approximately 410 nm (median ~240 nm). In contrast, the void size of the Co@NF-M electrode reduced to approximately 290 nm (median ~180 nm), while the Co@NF electrode exhibited even smaller voids, averaging approximately 180 nm (median ~130 nm). Although pristine NF exhibits a larger macropore diameter of approximately 65 μm (median ~50 μm), facilitating electrolyte transport, it presents a less developed surface morphology, which is inferred to provide a lower density of effective nucleation sites. This interpretation is consistent with the electrochemical results, where the NF-M-based electrodes exhibit reduced charge-transfer resistance (R_{ct}) and improved capacitive performance, indicating enhanced interfacial contact and more uniform active material deposition.

To quantitatively evaluate the effect of substrate engineering on surface development, nitrogen adsorption-desorption measurements were carried out. The pristine nickel foam (NF) exhibited a very low specific surface area of 0.08 $m^2\ g^{-1}$, consistent with its relatively smooth ligament structure and predominantly macroporous architecture. In contrast, the modified NF-M substrate exhibited a significantly higher specific surface area of approximately 15.3 $m^2\ g^{-1}$, indicating a substantial enhancement in surface development induced by the screen-printed Ni interlayer.

This pronounced increase in surface area is attributed to the formation of a hierarchical microstructure composed of nickel microparticles and surface protrusions, as evidenced by SEM analysis. Such features dramatically increase the density of high-energy surface sites (edges, steps, and defects), which act as preferential nucleation centers for cobalt growth. The BET results are therefore fully consistent with the observed improvement in nucleation uniformity and interfacial integration in the Co@NF-M electrode, confirming that the engineered substrate provides a significantly more favorable platform for heterogeneous nucleation and subsequent electrochemical activity.

Overall, the formation of a hierarchical nanosheet architecture was strongly promoted by the previously engineered nickel microparticle layer, which provided a high density of nucleation sites and facilitated

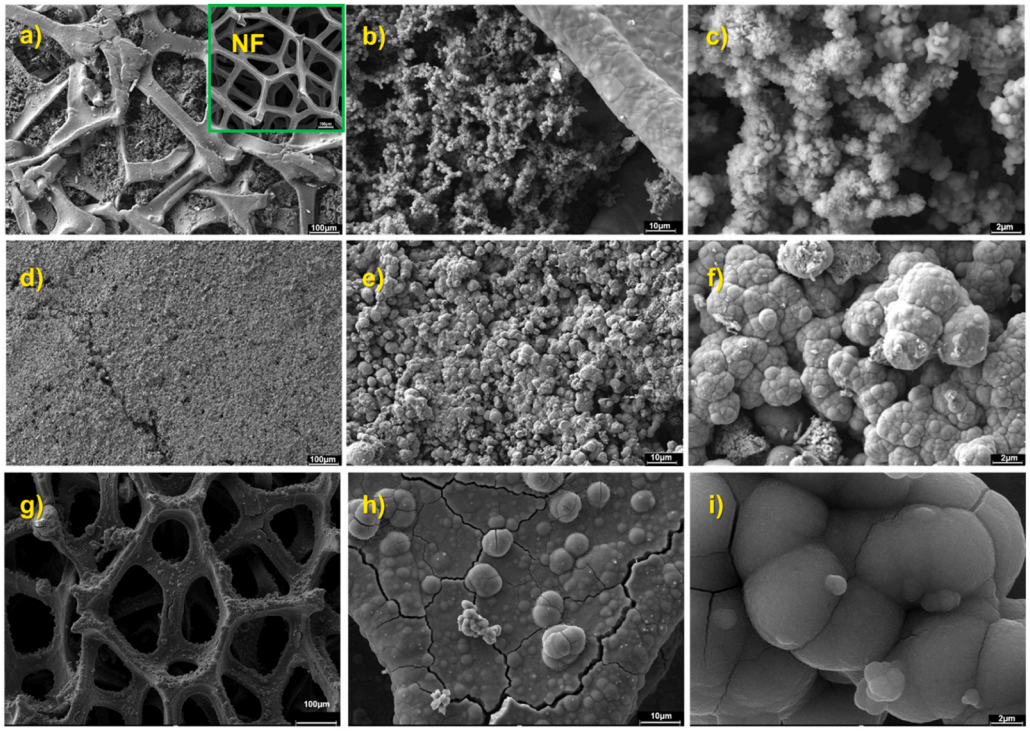

Fig. 1. FE-SEM images of the NF-M (a-c), inset NF (commercial nickel foam), Co@NF-M (d-f), and Co@NF (g-i) electrodes.

cobalt growth across the conductive scaffold. The intimate integration of Co nanostructures with a metallic Ni backbone ensures improved interfacial cohesion and robust mechanical stability. The interconnected metallic network provides continuous electron-transport pathways and increases the electrochemically accessible surface area, which contributes to the improved charge-transfer characteristics observed in the electrochemical measurements (see below).

Energy-dispersive X-ray spectroscopy (EDS) and elemental mapping were employed to investigate the surface composition and spatial distribution of elements in the fabricated electrodes (Figs. S1, S2). The EDS spectra confirmed the presence of Ni, Co, and O, verifying the successful deposition of cobalt-based species on the nickel foam substrates. For the modified nickel scaffold (NF-M), the spectrum is dominated by Ni (94.5 at%) with a minor oxygen contribution (5.5 at%), which can be attributed to the oxide layer typically formed on air-exposed nickel surfaces. After hydrothermal growth, the Co@NF-M electrode exhibited approximately 34.8 at% Co, 50.22 O, and 15.0 at% Ni. The presence of a detectable Ni signal indicates that the cobalt-based layer remains sufficiently porous to allow the partial detection of the underlying metallic framework. In contrast, the Co@NF electrode displayed a higher cobalt coverage (42.9 at% Co and 55.6 O) with only a minor Ni contribution (1.6 at%), suggesting a more continuous cobalt-based coating on the NF substrate. Elemental mapping of the Co@NF-M electrode further revealed a homogeneous spatial distribution of Co and O across the electrode surface, whereas Ni signals remained uniformly distributed beneath the coating. The coexistence and spatial overlap of the Co and Ni signals indicate intimate interfacial contact between the deposited layer and metallic substrate, which is favorable for efficient charge transfer during electrochemical cycling [38].

The crystalline structures of the NF-M and Co-deposited electrodes were examined using XRD (Fig. 2). The NF-M substrate exhibits characteristic reflections at 2θ ≈ 44.5°, 51.8°, and 76.4°, which can be indexed to the (111), (200), and (220) planes of face-centered cubic (fcc) metallic Ni (JCPDS 04–016–4761). No additional crystalline phases were detected by XRD. The sharp diffraction maxima indicate the good crystallinity of the metallic framework.

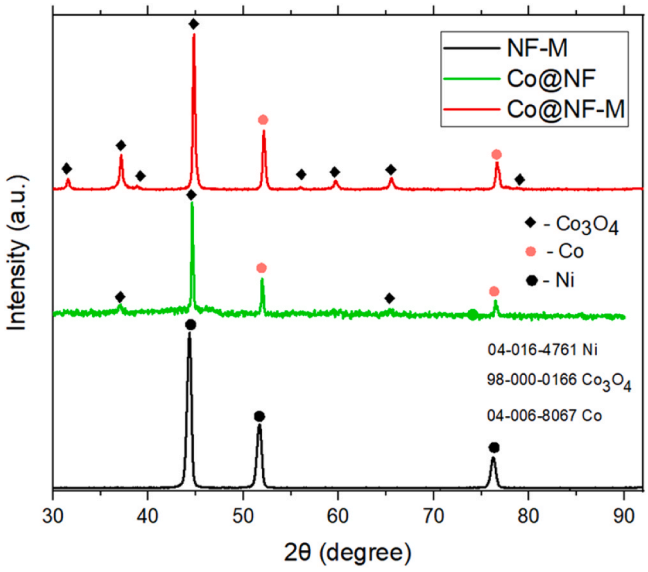

Fig. 2. XRD patterns of the Co@NF-M, Co@NF, and NF-M electrodes.

Following cobalt deposition, additional reflections appear at 2θ ≈ 19.0°, 31.3°, 36.8°, 44.8°, 59.3°, and 65.2°, corresponding to the (111), (220), (311), (400), (511), and (440) planes of spinel Co_3O_4 (JCPDS 98–000–0166). The observed reflection at approximately 44.8 °may include contributions from the Ni(111) substrate as well as the Co_3O_4 (400) plane. It is important to note that a minor contribution from metallic Co cannot be entirely excluded due to peak overlap in this region. Weak reflections corresponding to metallic Co (JCPDS 04–006–8067) were also observed, suggesting the partial coexistence of oxide and metallic cobalt phases. However, the identification of metallic Co remains tentative because of peak overlap and the limited sensitivity of XRD to minor or highly dispersed phases. Consequently, the XRD results primarily offer qualitative evidence for the formation of

crystalline Co_3O_4, while the presence of metallic Co, if any, is anticipated to be minor and cannot be reliably quantified using this technique. If present, metallic Co may contribute to improved electrical conductivity within the electrode, facilitating charge transport. In combination with the Co_3O_4 phase, which provides redox-active sites, this could lead to a synergistic enhancement of the electrochemical performance [39, 40].

The diffraction peaks assigned to Co_3O_4 were relatively sharp, indicating the good crystallinity of the deposited phase. The crystallite size was estimated using the Scherrer equation from the full width at half-maximum (FWHM) of the fitted diffraction peaks (Table S2). Based on the most intense Co_3O_4 (311) reflection at ~36.8°, the crystallite size of the Co@NF-M electrode was approximately 21.7 nm, indicating the formation of nanocrystalline cobalt oxide domains. Such nanoscale crystallites are beneficial for electrochemical energy storage because they shorten the ion-diffusion pathways and increase the density of electrochemically accessible active sites.

X-ray photoelectron spectroscopy (XPS) was also employed to investigate the surface chemical composition and oxidation states of the NF-M, Co@NF, and Co@NF-M electrodes (Fig. 3), with all binding energies calibrated to the C 1 s peak at 284.8 eV. The survey spectrum confirmed the presence of Ni, Co, O, and C, verifying the successful deposition of cobalt species on the nickel substrates (Fig. 3a). In the high-resolution Ni 2p spectra (Fig. 3b), two main peaks located at ~852.6 eV (Ni $2p_{3/2}$) and ~870.0 eV (Ni $2p_{1/2}$) were observed, together with shake-up satellite features at ~861.2 eV and ~879.6 eV. The detailed deconvolution of the Ni 2p spectra is presented in Fig. S3, confirming the coexistence of metallic Ni and surface oxidized nickel species. The spectra indicate the presence of the metallic Ni substrate together with surface oxidized nickel species, likely associated with a thin $NiO/Ni(OH)_2$ layer formed upon air exposure of the Ni framework [41,42]. For the cobalt-containing electrodes, the Co 2p spectra (Fig. 3c) displayed two prominent peaks centered at ~780.1 eV (Co $2p_{3/2}$) and ~795.3 eV (Co $2p_{1/2}$), together with satellite features at ~785.6 eV and ~802.4 eV, which are characteristic of mixed Co^{2+}/Co^{3+} states associated with the spinel Co_3O_4 phase [43]. This mixed-valence configuration plays a key role in charge storage. Specifically, the coexistence of Co^{2+} and Co^{3+} enables reversible Faradaic redox transitions [44]. The lower Co^{2+}/Co^{3+} ratio in Co@NF-M (1.4 vs 2.9 for Co@NF) indicates a more balanced mixed-valence surface, which is expected to facilitate reversible redox transitions and improved charge-transfer kinetics. This feature may facilitate enhanced charge transfer and is consistent with the larger CV area and lower charge transfer resistance (R_{ct}) observed in the electrochemical measurements (Section 3.2).

The O 1 s spectrum consists of a broad asymmetric peak that can be deconvoluted into three components (Fig. 3d). The component at ~529.6 eV corresponds to lattice oxygen (O^{2-}) associated with metal-oxygen bonds (Co-O and Ni-O); the peak at ~531.1 eV is attributed to surface hydroxyl groups (M-OH); and the higher binding energy component at ~532.6 eV originates from adsorbed water or oxygen-containing surface species [42,45]. The detailed deconvolution of the O 1 s spectra is presented in Fig. S5. Notably, the Co@NF sample exhibited a slight shift in the O 1 s peak toward higher binding energy compared with the NF-M substrate, indicating the modification of the oxygen coordination environment following cobalt deposition. This change reflects the formation of Co-O bonds and surface hydroxyl species typical of cobalt oxide/hydroxide nanostructures [46]. For the Co@NF-M electrode, the O 1 s envelope became more intense and

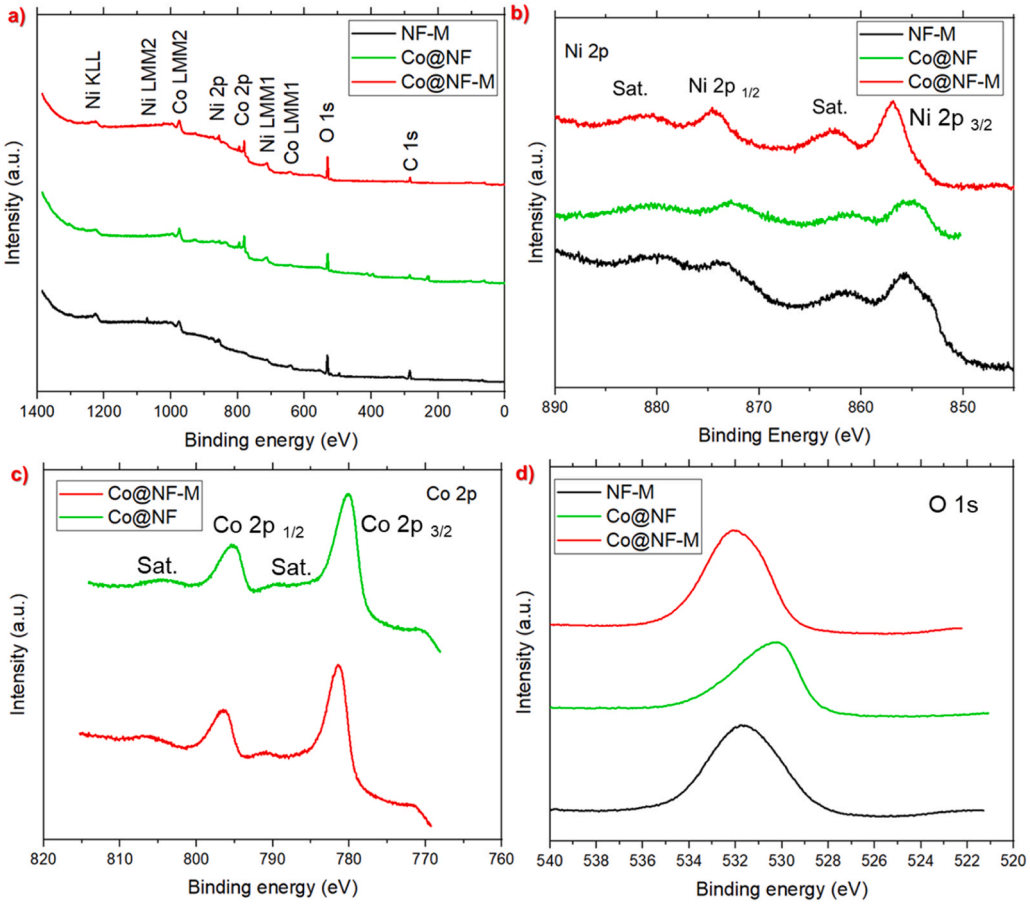

Fig. 3. XPS spectra of the NF-M, Co@NF, and Co@NF-M electrodes: survey spectra (a), and high-resolution spectra of Ni 2p (b), Co 2p (c), and O 1 s regions (d), confirming the presence of Ni, Co, and oxygen species associated with cobalt oxide formation on the nickel substrates.

slightly broadened, suggesting a higher concentration of surface oxygen species and hydroxyl groups [47]. These surface functionalities are known to facilitate pseudocapacitive reactions in alkaline electrolytes and may contribute to the improved electrochemical performance observed for the Co@NF-M electrode.

3.2. Electrochemical characterization

Various electrochemical experiments were performed using a 2 M KOH electrolyte to investigate the electrochemical characteristics of the fabricated electrodes. Fig. 4a presents the cyclic voltammetry test at 10 mV s^{-1}. The NF-M electrode exhibited a nearly rectangular CV profile with a low current response, indicating poor capacitive behavior and the absence of redox-active species. In contrast, the cobalt-modified electrodes displayed well-defined redox peaks corresponding to the reversible Co^{2+}/Co^{3+} and Co^{3+}/Co^{4+} transitions, confirming their pseudocapacitive nature [48]. The redox peaks confirm the Faradaic pseudocapacitive behavior associated with the reversible redox reactions of transition metal species in an alkaline electrolyte [49]. The Co^{2+}/Co^{3+} redox couple provides the dominant contribution to capacitance, while the Co^{3+}/Co^{4+} transition may contribute to higher potentials, enhancing the overall charge storage capability [50]. The substantially larger enclosed area of the Co@NF-M curve demonstrates its superior charge storage capacity and efficient redox kinetics compared with those of the Co@NF electrodes [51,52].

Kinetic analysis, based on the power-law relationship ($i = av^b$), further supports the above interpretation. The extracted b-value (~0.66) (Fig. S6) suggests a mixed charge storage mechanism that involves both surface-controlled and diffusion-controlled processes [53]. The deviation from ideal capacitive behavior (b = 1) implies that, alongside the rapid surface redox reactions linked to the Co^{2+}/Co^{3+} couple, a portion of the charge storage is derived from surface-controlled (pseudocapacitive) and diffusion-controlled processes [54]. This hybrid mechanism aligns with the hierarchical porous architecture, which facilitates electrolyte penetration and rapid surface reactions, while still allowing diffusion-limited processes within thicker regions of the active material.

To further clarify the electrolyte penetration mechanism within the hierarchical architecture, the ion transport process can be described in sequential steps, similar to the literature [55]. Initially, electrolyte ions are rapidly transported through the macroporous nickel foam scaffold, which acts as an open conductive framework enabling low-resistance ion access. Subsequently, ions infiltrate the interconnected nanosheet network, where mesoporous channels facilitate lateral ion diffusion toward electrochemically active sites. Finally, charge storage occurs via fast surface Faradaic reactions ($Co^{2+}/Co^{3+}/Co^{4+}$ redox transitions), while a fraction of ions penetrates deeper into the active material, giving rise to diffusion-controlled contributions.

This multi-scale transport process explains the intermediate b-value (~0.66), which reflects the coexistence of surface-controlled and diffusion-limited charge storage mechanisms within the hierarchical structure.

The Nyquist plot was obtained using electrochemical impedance spectroscopy (EIS) to further analyze the charge-transfer behavior and electrochemical kinetics of the as-prepared electrodes (Fig. 4b). The measurements were carried out over a frequency range of 10 mHz to 10 kHz using an AC perturbation of 10 mV. The intercept on the real (Z′) axis represents the combined internal resistance of the electrolyte and electrode (R_s) [56]. The diameter of the semicircle corresponds to the charge-transfer resistance (R_{ct}), which reflects the charge-transfer rate at the electrode-electrolyte interface [68]. The constant phase element (CPE) denotes the double-layer capacitance formed at the solid-liquid interface, while the Warburg element (Z_W) accounts for ion diffusion within the porous electrode structure [14,57].

The Co@NF-M electrode exhibits a much smaller semicircular diameter in the high-frequency region, signifying a reduced charge-transfer resistance (R_{ct} = 0.3 Ω cm^2), as shown in Table 1, and enhanced electrical conductivity due to the well-anchored cobalt species on the Ni foam, with a possible additional contribution from minor

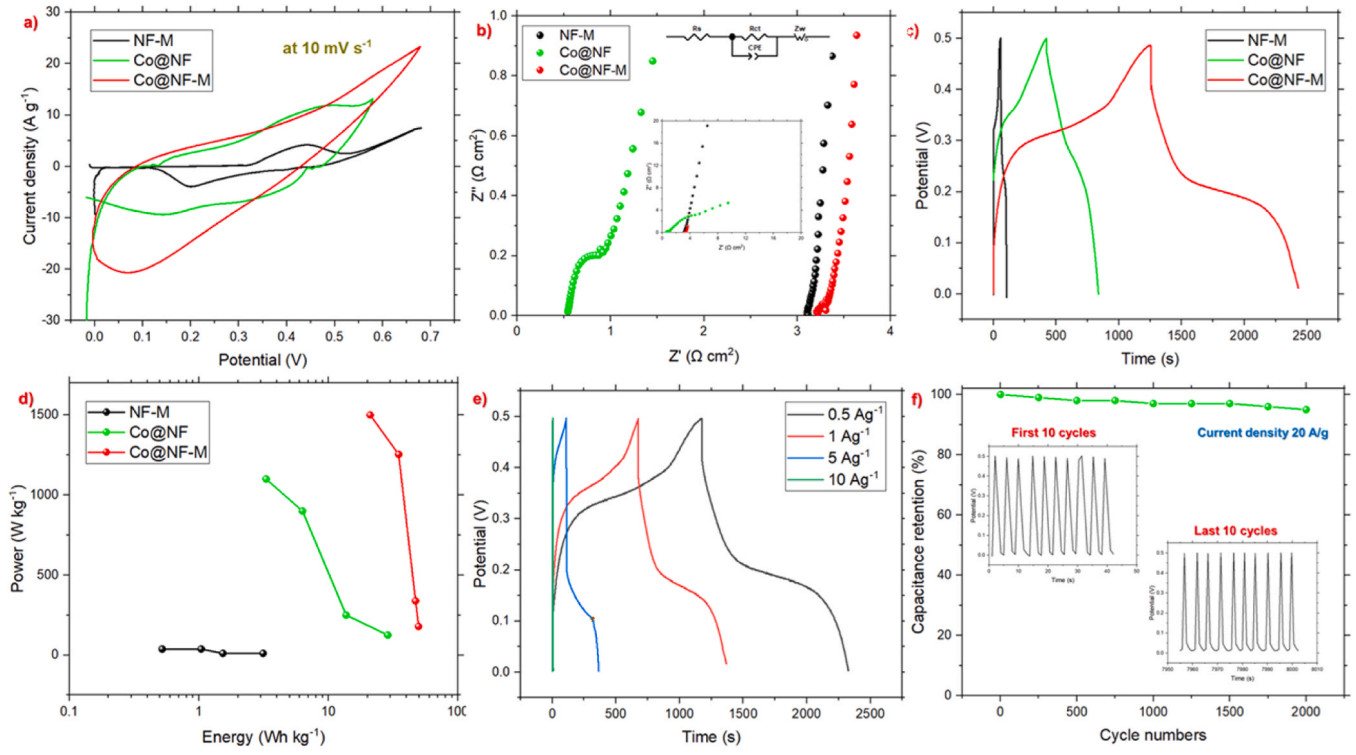

Fig. 4. Electrochemical evaluation of the as-prepared electrodes (NF-M, Co@NF, and Co@NF-M) in 2 M KOH: Cyclic voltammograms at 10 mV s^{-1} (a), Nyquist plot (b), GCD at 0.5 A g^{-1} (c), electrode-level Ragone estimate plot (d), GCD at various current densities for the Co@NF-M electrode (e), cycling stability test at 20 A g^{-1} of Co@NF-M for 2000 cycles with the first and last 10 cycles indicated in the inset (f).

Table 1
Equivalent circuit fitting parameters derived from electrochemical impedance spectroscopy (EIS) measurements for the NF-M, Co@NF, and Co@NF-M electrodes.

Electrode	R_s (Ω cm^2)	R_{ct} (Ω cm^2)	CPE-T (Ω^{-1} s^n)	CPE-P (n)	W-R	Chi-square χ^2
NF-M	3.12	0.62	0.007	0.77	1.23	0.0002
Co@NF	0.51	0.65	0.03	0.82	0.75	0.0015
Co@NF-M	3.02	0.32	0.01	0.88	0.46	0.00001

metallic Co domains that can facilitate electron transport within the electrode. The impedance spectra were fitted using a conventional equivalent circuit comprising R_s, R_{ct}, and a constant phase element (CPE). The nearly vertical line in the low-frequency region further indicates a quasi-capacitive behavior and efficient ion diffusion within the porous electrode network [58]. The Co@NF electrode exhibited an intermediate semicircle compared with NF-M and Co@NF-M, indicating improved charge-transfer properties after cobalt deposition, but it still had a higher interfacial resistance than the modified Co@NF-M electrode. In contrast, the NF-M electrode exhibited a larger semicircle, indicating sluggish charge transport and a limited electroactive surface area.

The enhanced EIS values can be directly attributed to the unique morphology of the Co@NF-M electrode. The interconnected nanosheet architecture developed on three-dimensional nickel foam creates a highly open and porous network that facilitates efficient electrolyte infiltration and reduces the number of ion diffusion pathways, in agreement with previous studies on structure-transport relationships in electrochemical systems [59]. Concurrently, the direct growth of the active material on a conductive substrate ensures robust interfacial contact, enabling rapid electron transport. Consequently, the optimized morphology effectively minimizes both the electron transport resistance and ion diffusion limitations, resulting in superior electrochemical performance.

In the GCD experiment at a current density of 0.5 A g^{-1} (Fig. 4c), Co@NF-M showed a much longer discharge time (1278 s) than the NF-M (138 s) and Co@NF (419 s) electrodes, directly indicating a far higher specific capacitance (C_s). The Co@NF-M curve is non-linear, with a broad plateau in the voltage range of ~0.42–0.18 V, a hallmark of pseudocapacitive Faradaic reactions (Co redox) rather than purely electric double-layer storage [60]. The slight nonlinearity of the GCD profiles suggests that charge storage is mainly governed by the reversible Faradaic redox reactions of the cobalt-based active phase [61]. Because the charge/discharge branches remained nearly symmetric and the operating voltage was limited to avoid significant gas-evolution processes, any contribution from side reactions was expected to be minor. Its initial IR drop at the start of discharge was relatively small, consistent with the low R_s observed in the Nyquist plot and with efficient electron/ion transport. The charge and discharge branches were nearly symmetric, indicating a high coulombic efficiency and good redox process reversibility [62]. In contrast, NF-M exhibited a short, nearly linear discharge with a pronounced slope, reflecting low capacitance and predominantly double-layer behavior on an essentially inert surface. Overall, Fig. 4c confirms that Co@NF-M delivers a higher capacitance, lower internal resistance, and more reversible kinetics than the bare substrate under identical conditions.

The specific capacitance (C_s) of each electrode was calculated using Eq. (1) [63] and the GCD curve shown in Fig. 4c:

$$Cs = \frac{I\,x\Delta t}{m\,x\Delta V} \quad (1)$$

where I is the constant discharge current (A), Δt is the discharge time (s), m is the mass of the active material (g), and ΔV is the potential window (V). The C_s values at 0.5 Ag^{-1} are 1278 Fg^{-1}, 419 Fg^{-1} and 138 Fg^{-1} for Co@NF-M, Co@NF, and NF-M, respectively. For comparison, a commercial NF electrode exhibits a specific capacitance of approximately 35 F g^{-1} at a current density of 0.5 A g^{-1} [14,64]. This low value highlights the limited intrinsic capacitive contribution of the nickel foam substrate and indicates that the enhanced capacitance of the Co@NF-M electrode arises from the combined effect of cobalt deposition and the modified NF scaffold structure.

Fig. 4d presents the variations in the energy and power density estimates derived from the three-electrode GCD data for the investigated electrodes. These values were used only to compare the rate-dependent charge-storage behavior of the individual electrodes. Co@NF-M maintains higher estimated energy values over the examined power range than Co@NF and NF-M, consistent with its higher specific capacitance and lower internal resistance. However, these results represent electrode-level behavior in a three-electrode configuration and should not be directly compared with the full-device Ragone metrics reported for practical two-electrode supercapacitors. The values of energy density (E) and power density (P) were determined using Eqs. (2) and (3), respectively [14,65,66]:

$$E = \frac{\frac{Cs*\Delta V^2}{2}}{3.6} \quad (2)$$

$$P = \frac{E * 3600}{\Delta t} \quad (3)$$

where C_s is the specific capacitance at each current density (F), ΔV is the potential range (V), and Δt is the discharge time (s).

Co@NF-M occupies the upper-right region of the map across the full range, indicating simultaneously higher energy and higher power than NF-M. As the power increased, the Co@NF-M energy decreased only gradually, which is a hallmark of low internal resistance and fast ion/electron transport (consistent with its small R_s and R_{ct} from EIS). The Co@NF electrode lies between NF-M and Co@NF-M in the Ragone plot, exhibiting significantly higher energy and power densities than the bare NF-M substrate but lower values than those of Co@NF-M. This intermediate behavior reflects the beneficial contribution of cobalt oxide to charge storage, while indicating that the untreated NF substrate provides less effective nucleation and electrical coupling than the modified NF-M scaffold. The NF-M points cluster in the lower-left, reflecting the poor charge-storage capability of the substrate and its inability to sustain high-rate operation [67]. The near-linear decay of energy with increasing power for Co@NF-M suggests a robust rate capability, even at the highest tested power, whereas NF shows marginal values throughout [68].

The Co@NF-M electrode delivered a maximum energy density of ~50 Wh kg^{-1} at a power density of ≈ 180 W kg^{-1}. As the current density increased, the power density rose to ~1500 W kg^{-1} while maintaining an energy density of ~21 Wh kg^{-1}, demonstrating good rate capability and efficient ion/electron transport. The Co@NF electrode exhibited intermediate performance, delivering higher energy and power densities than the bare NF-M substrate but lower values than Co@NF-M, demonstrating that cobalt oxide deposition significantly enhanced the charge-storage capability of the electrode. However, the improved performance of Co@NF-M suggests that the modified NF-M scaffold provides more effective nucleation sites and stronger electrical coupling between the cobalt oxide active material and the conductive substrate. In contrast, the bare NF electrode exhibited very low energy densities (<3 Wh kg^{-1}) and limited power performance owing to its poor electrochemical activity.

In addition, Fig. 4e presents the GCD of the Co@NF-M at various current densities. The obtained specific capacitances were 1278, 1184, 1003, and 602 Fg^{-1} at 0.5, 1, 5, and 10 Ag^{-1}, respectively. Notably, the long-term stability test (Fig. 4f) of Co@NF-M shows that 97% of the capacitance is retained after 2000 cycles at a current density of 20 Ag^{-1}. Furthermore, the morphology remained intact, as evidenced by the SEM

images taken after long-term stability testing (Fig. S7).

In the symmetric two-electrode configuration (Fig. S8), both electrodes consisted of Co@NF-M hydrothermally grown on NF-M substrates. This arrangement enabled an accurate evaluation of the overall electrochemical performance of the Co@NF-M material under realistic device conditions, as both electrodes contributed equally to charge storage. The electrodes were separated by a porous membrane, and an aqueous 2 M KOH solution was used as the electrolyte for the cell. This configuration reflects the practical operating mode of a complete supercapacitor cell, enabling the assessment of parameters such as energy and power densities and long-term cycling stability.

Initially, cyclic voltammetry was performed at different scan rates (Fig. 5a) to evaluate the electrochemical stability window and determine the maximum operating potential at which significant oxygen evolution did not occur. The results revealed that the potential window could be safely extended to 1.2 V, even without employing a carbon-based cathode. To ensure more reliable and safer experimental conditions, the test potential was set to 1.0 V.

Fig. 5b presents the cyclic voltammetry (CV) curves of the symmetric Co@NF-M//Co@NF-M device recorded at various scan rates ranging from 10 to 100 mV s^{-1} within the potential window of 0–1.0 V. All curves exhibit quasi-rectangular CVs with symmetrical shapes, even at higher scan rates, indicating excellent capacitive behavior and fast charge-discharge kinetics. The preservation of the CV shape with increasing scan rate demonstrates good rate capability and low internal resistance, indicating that the electrolyte ions can efficiently diffuse and access the active sites of both electrodes [69]. The slight increase in the current response with the scan rate further confirms the high reversibility and stability of the electrochemical process in the symmetric configuration [70].

Fig. 5c shows the galvanostatic charge-discharge (GCD) profiles of the symmetric Co@NF-M//Co@NF-M device measured at different current densities ranging from 5 to 40 mA cm^{-2} within a potential window of 1.0 V. All curves exhibited nearly triangular shapes with minimal iR drop, indicating ideal capacitive behavior and low internal resistance [71]. As the current density increased, the discharge time decreased, reflecting a good rate capability and fast ion transport within the electrode structure [72,73].

To calculate the areal capacitance, Eq. (4) was used:

$$C_A = \frac{J * \Delta t}{\Delta V} \tag{4}$$

Where, C_A is the areal capacitance (F cm^{-2}), J is the current density (A cm^{-2}), Δt is the discharge time (s), and ΔV is the potential window excluding IR drop (V).

The areal capacitance values derived from the galvanostatic discharge profiles were approximately 4740, 2660, 920, and 160 mF cm^{-2} at current densities of 5, 10, 20, and 40 mA cm^{-2}, respectively. The obtained values are competitive with or exceed those of several reported cobalt-containing systems (Table S3). Although the capacitance gradually decreases with increasing current density owing to enhanced polarization and diffusion constraints, the device retains a significant fraction of its charge-storage capability even at elevated rates. This behavior reflects efficient electrolyte-ion transport within the porous electrode network and rapid Faradaic kinetics at the Co-based active sites. The sustained capacitance under high-current operation highlights the favorable rate capability of the symmetric Co@NF-M//Co@NF-M configuration and underscores the structural and electrochemical robustness of the integrated electrode architecture.

Fig. 5d shows the long-term cycling stability of the symmetric Co@NF-M//Co@NF-M supercapacitor, evaluated through continuous charge-discharge cycling at a constant current density (30 mA cm^{-2}). The capacitance retention remained remarkably high throughout the 3000-cycle test, maintaining approximately 95% of the initial

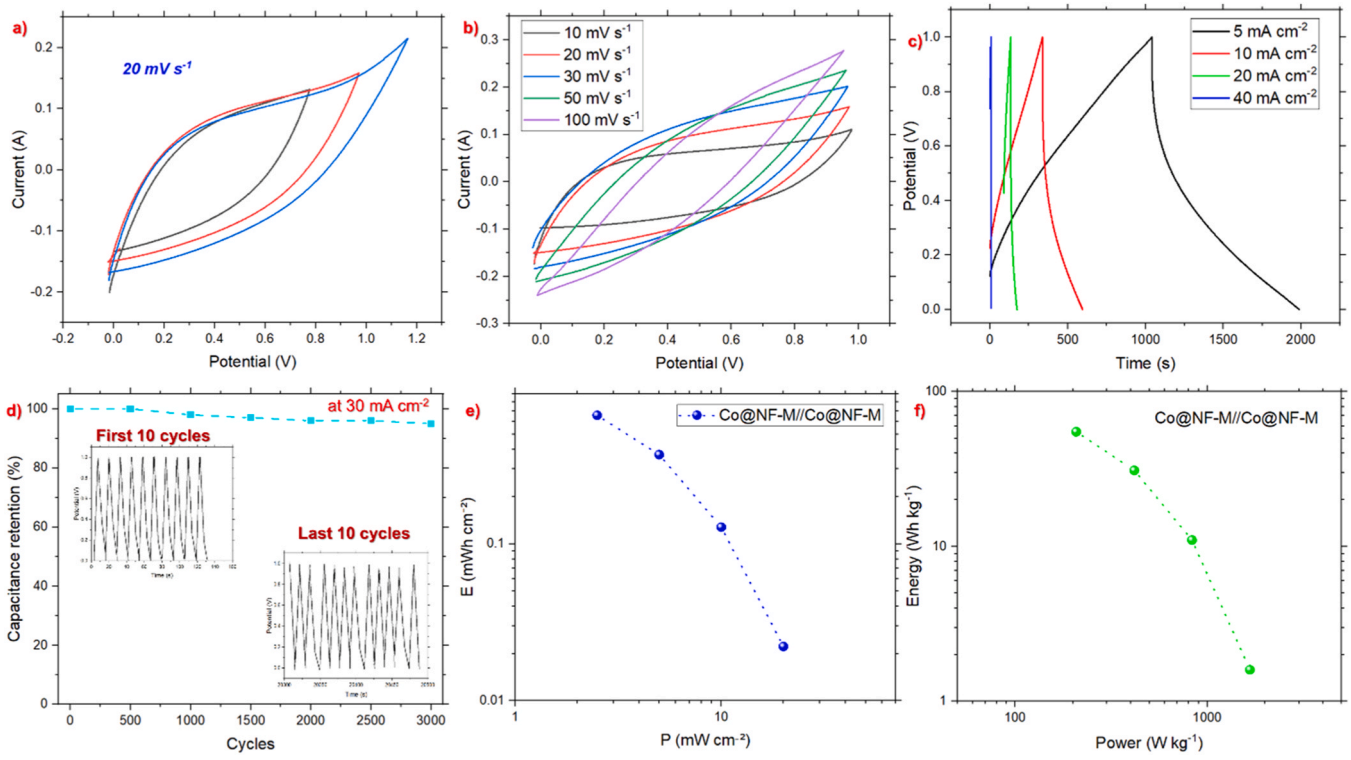

Fig. 5. Electrochemical performance of the symmetric Co@NF-M//Co@NF-M supercapacitor in a two-electrode configuration (2 M KOH electrolyte). Cyclic voltammetry curves recorded at 20 mV s^{-1} within various operating potential windows (a), CV profiles at various scan rates (10–100 mV s^{-1}), demonstrating the rate capability and charge-storage kinetics of the device (b), Galvanostatic charge-discharge curves measured at various current densities (c), Cycling stability evaluated at 30 mA cm^{-2} over 3000 cycles, with the first and last 10 charge-discharge cycles shown in the insets (d), Areal Ragone plot (e), Gravimetric Ragone plot of the symmetric calculated based on the total active mass of both electrodes (f).

capacitance after prolonged operation. This excellent stability demonstrates the strong structural integrity and adhesion of the Co-based active material to the NF-M substrate, preventing significant degradation or detachment during repeated redox reactions. In addition, the coulombic efficiency (CE) was calculated as the ratio of discharge to charge time, stabilizing at approximately 96.5% after the initial activation cycles and remaining nearly constant throughout prolonged cycling (Fig. S9). This indicates predominantly reversible charge storage with minor irreversible contributions, likely arising from Faradaic redox processes and limited side reactions. The high and stable coulombic efficiency, together with excellent capacitance retention, confirms the robust electrochemical reversibility and structural stability of the electrode.

To find the correlation between the energy density and power density of the symmetric cell, Eqs. (5 and 6) were used:

$$E_A = \frac{1}{2} C_A * (\Delta V)^2 \tag{5}$$

$$P_A = \frac{E_A * 3600}{\Delta t} \tag{6}$$

Where E_A is the energy density (Wh cm^{-2}), C_A is the areal capacitance (F cm^{-2}), ΔV is the device voltage window (V), P_A is the power density (W cm^{-2}), and Δt is the discharge time (s).

The areal Ragone plot of the symmetric Co@NF-M//Co@NF-M device (Fig. 5e), derived from galvanostatic charge-discharge measurements, demonstrates an energy density of ~0.66 mWh cm^{-2} at a power density of ~2.5 mW cm^{-2}, maintaining ~0.02 mWh cm^{-2} even at ~20 mW cm^{-2}, indicating a good rate capability. The Co@NF-M//Co@NF-M device outperformed several previously reported supercapacitor systems, such as metal-free polymer electrodes (0.40 mWh cm^{-2}) [9,74] and rGO@$CuCo_2O_4$ electrodes (0.2 mWh/cm^{-2}) [75]. The corresponding gravimetric Ragone plot (Fig. 5f) further confirms the energy-power characteristics of the device. The Co@NF-M//Co@NF-M symmetric supercapacitor delivered a high energy density of ~54.9 Wh kg^{-1} at a power density of ~208 W kg^{-1}, while retaining ~1.85 Wh kg^{-1} at ~1667 W kg^{-1}. These results demonstrate that the device maintains an appreciable energy storage capability even at a high power output, highlighting its favorable rate performance.

4. Conclusion

In this work, cobalt nanostructures were directly grown on a microstructurally engineered nickel foam substrate via a two-step fabrication strategy comprising substrate modification and hydrothermal deposition of cobalt. Structural and surface analyses confirmed the formation of crystalline Co3O4 uniformly distributed across the modified Ni framework. Electrochemical impedance spectroscopy further demonstrated a reduced charge transfer resistance for the Co@NF-M electrode compared to the electrodes prepared on commercial nickel foam, indicating improved interfacial charge transport within the electrode structure.

Electrochemical evaluation showed that the Co@NF-M electrode delivered a specific capacitance of 1184 F g^{-1} at 1 A g^{-1} in a three-electrode configuration, significantly exceeding the performance of the corresponding Co@NF and NF-M electrodes. When assembled into a symmetric Co@NF-M//Co@NF-M device, the system operated stably within a 1.0 V potential window, achieving an areal capacitance of 4740 mF cm^{-2} at 5 mA cm^{-2} and retaining 95% of its initial capacitance after 3000 cycles, demonstrating excellent electrochemical stability and rate capability.

These results show that the combination of an engineered nickel scaffold and cobalt oxide nanostructures directly grown on it yields improved electrochemical performance compared with electrodes prepared using commercial nickel foam. The two-step fabrication strategy enables the formation of a hierarchical electrode architecture in which the modified metallic substrate and cobalt oxide active phase function together to support efficient charge storage.

This study highlights the importance of current-collector engineering as a complementary design parameter, demonstrating that the controlled modification of the metallic scaffold prior to active-material growth can provide an effective pathway to enhance the performance of transition-metal-oxide electrodes in electrochemical energy-storage devices. Designing hierarchical metallic scaffolds that simultaneously provide mechanical support and efficient transport pathways is a promising strategy for improving the performance of electrochemical electrodes.

CRediT authorship contribution statement

Pavel Shuhayeu: Writing – review & editing, Data curation, Conceptualization. **Jarosław Milewski:** Writing – review & editing, Supervision, Resources, Project administration, Funding acquisition, Data curation. **Karolina Majewska:** Writing – review & editing, Data curation, Conceptualization. **Ioannis Poimenidis:** Writing – review & editing, Writing – original draft, Visualization, Validation, Methodology, Investigation, Formal analysis, Data curation, Conceptualization. **Kamil Bochenek:** Writing – review & editing, Methodology, Data curation, Conceptualization. **Aliaksandr Martsinchyk:** Writing – review & editing, Data curation, Conceptualization. **Michalis Konsolakis:** Writing – review & editing, Validation, Supervision, Resources, Project administration, Methodology, Formal analysis.

Declaration of Competing Interest

The authors declare that they have no known competing financial interests or personal relationships that could have appeared to influence the work reported in this paper.

Acknowledgements

The authors would like to thank M. Sc. Mateusz Włoczewski (Institute of Fundamental Technological Research of the Polish Academy of Sciences) for his help with the XRD analysis, and Dr. Evangelia Skliri (IESL-Greece) for the XPS analysis. This research was partially funded by the Warsaw University of Technology within the Excellence Initiative: Research University (IDUB) program.

Appendix A. Supporting information

Supplementary data associated with this article can be found in the online version at doi:10.1016/j.nxmate.2026.102264.

Data Availability

The data supporting the findings of this study are available from the corresponding author upon reasonable request.

References

[1] A. Gupta, S. Suhag, Evaluation of energy storage systems for sustainable development of renewable energy systems—A comprehensive review, J. Renew. Sustain. Energy 14 (2022).
[2] N. Parveen, Resent development of binder-free electrodes of transition metal oxides and nanohybrids for high performance supercapacitors – a review, Chem. Rec. 24 (2024).
[3] C. Lian, D. Jiang, H. Liu, J. Wu, A generic model for electric double layers in porous electrodes, J. Phys. Chem. C. 120 (2016) 8704–8710.
[4] S. Witomska, et al., Graphene oxide hybrid with sulfur–nitrogen polymer for high-performance pseudocapacitors, J. Am. Chem. Soc. 141 (2019) 482–487.
[5] V. Augustyn, P. Simon, B. Dunn, Pseudocapacitive oxide materials for high-rate electrochemical energy storage, 1597–1597, Energy Environ. Sci. 7 (2014), 1597–1597.

[6] C. Yi, J. Zou, H. Yang, X. Leng, Recent advances in pseudocapacitor electrode materials: Transition metal oxides and nitrides, Trans. Nonferrous Met. Soc. China 28 (2018) 1980–2001.
[7] T. Cottineau, M. Toupin, T. Delahaye, T. Brousse, D. Bélanger, Nanostructured transition metal oxides for aqueous hybrid electrochemical supercapacitors, Appl. Phys. A 82 (2006) 599–606.
[8] S. Jayakumar, P.C. Santhosh, M.M. Mohideen, A.V. Radhamani, A comprehensive review of metal oxides (RuO2, Co3O4, MnO2 and NiO) for supercapacitor applications and global market trends, J. Alloy. Compd. 976 (2024) 173170.
[9] I.A. Poimenidis, P.A. Loukakos, M. Konsolakis, NiO nanolayer electrodeposited with Cobalt and Phosphide as a novel supercapacitor with high areal capacitance, 112365–112365, J. Phys. Chem. Solids 196 (2025), 112365–112365.
[10] X. Bai, et al., Hierarchical Co3O4@Ni(OH)2 core-shell nanosheet arrays for isolated all-solid state supercapacitor electrodes with superior electrochemical performance, Chem. Eng. J. 315 (2017) 35–45.
[11] G.-H. Ao, et al., Construction of Hierarchical Porous Architecture on Ni Foam for Efficient Oxygen Evolution Reaction Electrode, Front. Mater. 8 (2021) 726270.
[12] M.S. Ratsoma, et al., Application of Nickel Foam in Electrochemical Systems: A Review, J. Electron. Mater. 52 (2023) 2264–2291.
[13] J. Zhang, W. Zhang, L. Xing, H. Su, Q. Xu, Experimental investigation on the effect of mixed acids etched nickel foam electrode on performance of an alkaline direct ethanol fuel cell, E3S Web Conf. 194 (2020) 02021.
[14] I.A. Poimenidis, M. Lykaki, P.A. Loukakos, M. Konsolakis, Ultra-high supercapacitor performance of NiSRu@NiO nanocomposites on nickel foam electrodes, 110679–110679, J. Energy Storage 83 (2024), 110679–110679.
[15] I.A. Poimenidis, et al., Electrodeposited Ni foam electrodes for increased hydrogen production in alkaline electrolysis, 127798–127798, Fuel 342 (2023), 127798–127798.
[16] Z. Zhang, et al., An electrochemical modification strategy to fabricate NiFeCuPt polymetallic carbon matrices on nickel foam as stable electrocatalysts for water splitting, Chem. Sci. 13 (2022) 8876–8884.
[17] R. Walden, et al., Nonthermal plasma technologies for advanced functional material processing and current applications: Opportunities and challenges, J. Environ. Chem. Eng. 12 (2024) 113541.
[18] I.A. Poimenidis, et al., Ni foam electrodes decorated with Ni nanoparticles via pulsed laser deposition for efficient hydrogen evolution reaction, 116922–116922, Mater. Sci. Eng. B 299 (2024), 116922–116922.
[19] I. Poimenidis, et al., in: A.V. Kabashin, M. Farsari, M. Mahjouri-Samani (Eds.), Laser-nanostructured substrates for enhanced hydrogen evolution reaction, SPIE, 2024, https://doi.org/10.1117/12.3003827, 1–1.
[20] I. Poimenidis, et al., Laser-nanostructured Ni-Fe electrodes for improved supercapacitor-electrolysers systems, 116599–116599, Mater. Sci. Eng. B 295 (2023), 116599–116599.
[21] I.A. Poimenidis, et al., Electrodeposited laser – nanostructured electrodes for increased hydrogen production, Int. J. Hydrog. Energy 47 (2022) 9527–9536.
[22] D. Yan, et al., High-Performance sodium-ion capacitors with kinetics-matched characteristics enabled by N/O/S-doped homologous carbon electrodes derived from a single precursor, Rare Met 45 (2026) e70033.
[23] J.N. Hausmann, et al., In-liquid plasma modified nickel foam: NiOOH/NiFeOOH active site multiplication for electrocatalytic alcohol, aldehyde, and water oxidation, Adv. Energy Mater. 12 (2022) 2202098.
[24] Y. Ma, et al., Aprotic solvent-assisted local Lewis acid etching for the efficient doping of Cu ions into Ni foam with enhanced electrochemical sensing performance, Microchem. J. 224 (2026) 117829.
[25] A. Tahir, et al., Surface engineering of nickel foam for cost-effective and highly corrosion-resistant electrodes for water and seawater electrolysis, J. Ind. Eng. Chem. 153 (2026) 691–702.
[26] D. Cai, et al., Interface-oriented engineering of bio-fermented bamboo-derived carbon via F/O doping for advanced sodium-ion storage, J. Energy Storage 141 (2026) 119444.
[27] S. Karthika, T.K. Radhakrishnan, P. Kalaichelvi, A Review of Classical and Nonclassical Nucleation Theories, Cryst. Growth Des. 16 (2016) 6663–6681.
[28] K. Wang, K.N. Hui, K. San Hui, S. Peng, Y. Xu, Recent progress in metal–organic framework/graphene-derived materials for energy storage and conversion: design, preparation, and application, Chem. Sci. 12 (2021) 5737–5766.
[29] T. Wejrzanowski, et al., Metallic foam supported electrodes for molten carbonate fuel cells, Mater. Des. 193 (2020) 108864.
[30] Nelson Castro, Nelson Pereira, Vanessa F. Cardoso, Clarisse Ribeiro, Senentxu Lanceros-Mendez. Micro- and nanostructured piezoelectric polymers, Elsevier, 2019, pp. 35–65. Frontiers of Nanoscience14.
[31] M.F.L. Garcia, et al., Binder-free Co3O4 sheet-like morphology on 3D nickel foam for efficient alkaline water electrolysis, J. Phys. Chem. Solids 208 (2026) 113203.
[32] H.Y. Hoang, N.T. Hoang, B.D. Nhi, H. Le-Quoc, H. Van Nam, Nickel foam-based electrode materials for multifunctional electrochemical applications: from substrate to active platform, J. Environ. Chem. Eng. 13 (2025) 118695.
[33] I. Poimenidis, E. Skliri, V. Binas, K. Komnitsas, M. Konsolakis, Hydrothermal growth of Co3O4 nanoparticles on nickel foam for high-performance pseudocapacitive supercapacitors: Effect of cobalt loading, Mater 10 (2026) 101449.
[34] I.A. Poimenidis, M. Lykaki, S. Moustaizis, P. Loukakos, M. Konsolakis, One-step solvothermal growth of NiO nanoparticles on nickel foam as a highly efficient electrocatalyst for hydrogen evolution reaction, 128007–128007, Mater. Chem. Phys. 305 (2023), 128007–128007.
[35] S. Khokhar, P. Chand, H. Anand, Probing the effect of electrolyte ions on the electrochemical performance of nickel-based metal-organic frameworks, Mater. Chem. Phys. 330 (2025) 130144.
[36] B. Brioual, et al., Influence of the concentration of KOH-based aqueous electrolyte on the electrochemical behavior of NiO thin film, J. Indian Chem. Soc. 101 (2024) 101170.
[37] G. Sriram, et al., Recent trends in hierarchical electrode materials in supercapacitor: Synthesis, electrochemical measurements, performance and their charge-storage mechanism, J. Energy Storage 94 (2024) 112454.
[38] X. Wang, Oxygen catalytic evolution reaction on nickel hydroxide electrode modified by electroless cobalt coating, Int. J. Hydrog. Energy 29 (2004) 967–972.
[39] D. Wang, et al., Co@Co_3O_4 Prepared in Situ from Metallic Co as an Efficient Semiconductor Catalyst for Photocatalytic Water Oxidation, ACS Sustain. Chem. Eng. 6 (2018) 8300–8307.
[40] S. Shinde, A.R. Kumar, Advances in Cobalt Oxide-Based Supercapacitors: Recent Strategies and Performance Enhancement, ChemistrySelect 10 (2025) e01497.
[41] A.P. Grosvenor, M.C. Biesinger, R.St.C. Smart, N.S. McIntyre, New interpretations of XPS spectra of nickel metal and oxides, Surf. Sci. 600 (2006) 1771–1779.
[42] J. Shen, et al., Heteroatom modification of nanoporous nickel surfaces for electrocatalytic water splitting, ACS Appl. Nano Mater. 3 (2020) 11298–11306.
[43] Q. Duan, H. Chen, Synthesis and electrochemical properties of Co_3O_4 nanoparticles by hydrothermal method at different temperatures, IOP Conf. Ser. Mater. Sci. Eng. 207 (2017) 012020.
[44] S.-S. Li, et al., Engineering Co2+/Co3+ redox activity of Ni-mediated porous Co3O4 nanosheets for superior Hg(II) electrochemical sensing: insight into the effect of valence change cycle and oxygen vacancy on electroanalysis, Sens. Actuators B Chem. 354 (2022) 131095.
[45] M. Baranov, et al., Entrapment of metastable nanocrystals by polyoxometalates, Chem. Commun. 59 (2023) 4364–4367.
[46] J. Fester, et al., Edge reactivity and water-assisted dissociation on cobalt oxide nanoislands, Nat. Commun. 8 (2017) 14169.
[47] G. Yang, J. Kim, B. Lee, J.E. Jang, H. Kwon, One-step laser-induced oxidation and doping for tailored p-type conversion of Al-doped TiO_2, Small 21 (2025) 2502139.
[48] D. Merum, et al., Impact of Co-doping on the microstructural and electrochemical features of mesoporous 3D oval–shaped Ni3-xCoxV2O8 electrodes for high-performance hybrid supercapacitors, J. Energy Storage 61 (2023) 106674.
[49] Y. Cai, et al., Dual-site Zn doping boosts longevity and air stability of O3-type NaNi1/3Fe1/3Mn1/3O2 cathode for high-performance sodium-ion batteries, J. Power Sources 631 (2025) 236272.
[50] Y.-C. Huang, et al., *In Situ / Operando* Soft X-ray spectroscopic identification of a Co^{4+} intermediate in the oxygen evolution reaction of defective Co_3O_4 nanosheets, J. Phys. Chem. Lett. 13 (2022) 8386–8396.
[51] H. Wang, et al., Novel DEalloying-fabricated NiS/NiO nanoparticles with superior cycling stability for supercapacitors, ACS Omega 6 (2021) 17999–18007.
[52] X. Yin, et al., A novel structure of Ni-(MoS 2 /GO) composite coatings deposited on Ni foam under supergravity field as efficient hydrogen evolution reaction catalysts in alkaline solution, Electrochim. Acta 249 (2017) 52–63.
[53] J. Song, et al., Synergistic effects of P-functionalization and localized graphitization in sustainable hard carbon for enhanced sodium and potassium storage, J. Colloid Interface Sci. 686 (2025) 1200–1214.
[54] X. Deng, et al., Renewable carbon foam/δ-MnO2 composites with well-defined hierarchical microstructure as supercapacitor electrodes, J. Mater. Res. Technol. 9 (2020) 8544–8555.
[55] W. Yu, et al., Understanding multi-scale ion-transport in solid-state lithium batteries, eScience 5 (2025) 100278.
[56] J. Chen, et al., Enhanced lithium storage capability enabled by metal nickel dotted NiO–graphene composites, J. Mater. Sci. 54 (2019) 1475–1487.
[57] B.E. Conway, V. Birss, J. Wojtowicz, The role and utilization of pseudocapacitance for energy storage by supercapacitors, J. Power Sources 66 (1997) 1–14.
[58] X. Ren, et al., Electrostatically induced intercalation of layered double hydroxide in graphene oxide for enhanced electrochemical energy storage, Adv. Sci. (2025) e15923, https://doi.org/10.1002/advs.202515923.
[59] D. Cai, et al., Gradient SEI and interfacial polarization orchestrate Na+ kinetics in heteroatom-engineered hard carbon, Chem. Eng. J. 529 (2026) 173065.
[60] G.Z. Chen, Linear and non-linear pseudocapacitances with or without diffusion control, Prog. Nat. Sci. Mater. Int. 31 (2021) 792–800.
[61] P. Kumcham, et al., Architecting cobalt molybdate nanostructures via urea tuning: promising battery-type electrodes for high energy density hybrid supercapacitors, J. Phys. Chem. Solids (2026) 113764, https://doi.org/10.1016/j.jpcs.2026.113764.
[62] C. Cougnon, Exploring the interdependence between the coulombic, voltage and energy efficiencies, Electrochem. Commun. 120 (2020) 106832.
[63] K. Xu, et al., Hierarchical mesoporous NiCo2O4@MnO2 core–shell nanowire arrays on nickel foam for aqueous asymmetric supercapacitors, 4795–4795, J. Mater. Chem. A 2 (2014), 4795–4795.
[64] B. Pierożyński, M. Kuczyński, T. Mikołajczyk, Simple nickel foam modification procedures for enhanced Ni foam supercapacitor applications, Crystals 14 (2024) 777.
[65] F.Z. Amir, V.H. Pham, J.H. Dickerson, Facile synthesis of ultra-small ruthenium oxide nanoparticles anchored on reduced graphene oxide nanosheets for high-performance supercapacitors, RSC Adv. 5 (2015) 67638–67645.
[66] K. Chaitra, et al., High energy density performance of hydrothermally produced hydrous ruthenium oxide/multiwalled carbon nanotubes composite: design of an asymmetric supercapacitor with excellent cycle life, J. Energy Chem. 25 (2016) 627–635.
[67] G.A. Elia, N.A. Kyeremateng, K. Marquardt, R. Hahn, An aluminum/graphite battery with ultra-high rate capability, Batter. Supercaps 2 (2019) 83–90.

[68] Z.-Y. Li, et al., Unveiling the role of Co in improving the high-rate capability and cycling performance of layered $Na_{0.7}$ $Mn_{0.7}$ Ni $_{0.3-x}$ Co $_x$ O_2 cathode materials for sodium-ion batteries, ACS Appl. Mater. Interfaces 8 (2016) 15439–15448.
[69] K. Boukhouidem, et al., Ternary WO_3–MnO_2@SiNWs hybrid electrodes for high-performance Micro-supercapacitors with enhanced energy density and stability, J. Electroanal. Chem. 999 (2025) 119559.
[70] C. Wang, et al., Design of efficient, reliable, and wide-band filter electrochemical capacitors via matching positive with negative electrodes, Joule 8 (2024) 764–779.
[71] R.A. Kadam, et al., Enhanced electrochemical performance of cobalt vanadium oxide supercapacitors through optimized reduced graphene oxide composite, Mater. Charact. 229 (2025) 115640.
[72] S. Geng, J. Zhou, B. Tan, B. Zheng, K. Zhang, Impact of thickness and charge rate on the electrochemical performance of Si-based electrodes, Cell Rep. Phys. Sci. 5 (2024) 102305.
[73] H. Pan, et al., Supercapacitor with Ultra-High power and energy density enabled by Nitrogen/Oxygen-Doped interconnected hollow carbon Nano-Onions, Chem. Eng. J. 484 (2024) 149663.
[74] Z. Roohi, F. Mighri, Z. Zhang, A flexible, lightweight, and high-performance supercapacitor made of nanofibrous polypyrrole electrodes, ACS Omega 10 (2025) 31600–31609.
[75] C. Fang, D. Zhang, High multifunctional performance structural supercapacitor with Polyethylene oxide cement electrolyte and reduced graphene oxide@ CuCo2O4 nanowires, Electrochim. Acta 401 (2022) 139491.